Physica Scripta

PAPER

Complex diagnostic and numerical study of x-ray and particle emissions under relativistic ultra-short laser-solid interaction

Ehsan Eftekhari-Zadeh[1,2,3,*], **Robert Loetzsch**[1,2], **Lorenzo Manganelli**[4], **Manuel Sebastian Blümcke**[1], **Anna Tauschwitz**[4], **Ingo Uschmann**[1,2], **Alexander Pukhov**[5], **Olga Rosmej**[4,6], **Christian Spielmann**[1,2,3] and **Daniil Kartashov**[1,3]

[1] Institute of Optics and Quantum Electronics, Friedrich Schiller University Jena, Max-Wien-Platz 1, 07743 Jena, Germany
[2] Helmholtz Institute Jena, Fröbelstieg 3, 07743 Jena, Germany
[3] Abbe Center of Photonics, Friedrich Schiller University Jena, Albert Einstein Straße 6, 07745 Jena, Germany
[4] Goethe University, Max-von-Laue-Strasse 1, 60438 Frankfurt am Main, Germany
[5] Institut für Theoretische Physik I, Heinrich-Heine-Universität Düsseldorf, D-40225 Dusseldorf, Germany
[6] Plasma Physics Department, GSI Helmholtz Center for Heavy Ion Research, 64291 Darmstadt, Germany
[*] Author to whom any correspondence should be addressed.

E-mail: e.eftekharizadeh@uni-jena.de

Keywords: relativistic laser-solid interaction, high power lasers, x-rays and particle generations, x-ray spectroscopy, laser energy absorption in plasmas, transient plasmas, hole boring

OPEN ACCESS

RECEIVED
4 April 2023

REVISED
19 June 2023

ACCEPTED FOR PUBLICATION
3 October 2023

PUBLISHED
19 October 2023

Abstract

In this report, we present the experimental results on the generation of x-ray emission and particle acceleration using high temporal contrast ($\sim 10^{-9}$ at picosecond time scale), ultrashort ($\sim 30fs$), relativistic ($a_0 \approx 5$) near-IR laser pulses interacting with Titanium foils. Complex diagnostics, including the energy spectra of accelerated electrons from both front and rear target sides, electron angular distribution and x-ray spectroscopy of the plasma emission were employed. Analysis of the characteristic radiation produced by highly charged Ti^{+20} ions led to the conclusion that laser-plasma interaction, which leads to the generation of keV hot plasma, occurs at plasma densities 10x higher than relativistic critical electron density. Numerical simulations, including hydrodynamic calculations to model pre-plasma, generated on nanosecond-picosecond time scale under our experimental conditions and relativistic particle-in-cell simulations for main pulse interaction with the plasma reproduce well electron energy and angular distributions. They show the onset of hole boring effect under near normal incidence that leads to plasma density steepening and enables penetration of high intensity laser radiation into the overcritical plasma to much higher densities (up to 30 n_{cr}), what is in a good agreement with the results of x-ray spectroscopy.

1. Introduction

The developments in the table-top terawatt lasers, based on the Chirped Pulse Amplification technique (CPA) introduced more than thirty years ago (Strickland and Mourou 1985), have opened up a revolutionary era in High Energy Density Physics (HEDP) enabling us to address some of the most fundamental questions regarding light–matter interaction and to study matter at extreme conditions on the ultrashort timescale at intensities in which the motion of electrons is governed totally by relativistic effects (Kumar 2010). Such university-scale laboratory lasers have emerged as attractive tools among researchers particularly over the last few decades due to their exceptional potentials in numerous applications. They are being widely employed in laboratory astrophysics (Huang *et al* 2019, Parigger 2020), fast ignition in Inertial Confinement Fusion (ICF) (Roth *et al* 2001, Kemp *et al* 2014), medical therapy (Bulanov and Khoroshkov 2002, Ledingham *et al* 2007, Karsch 2017) and medical isotope production (Ma *et al* 2019), neutron radiography and tomography (Strobl *et al* 2009), charged particle production and acceleration (Macchi *et al* 2013, Yogo *et al* 2017, Higginson *et al* 2018, Rosmej *et al* 2019), x-ray and gamma ray production (Rousse *et al* 2004, Chang *et al* 2017, Rosmej *et al* 2019), and so forth.

The process of intense laser radiation—solid interaction is extremely complex and strongly depends on parameters of the radiation (intensity, pulse duration, wavelength, polarization), focusing geometry, and characteristics of the solid (material, thickness, morphology of the surface etc.) (Umstadter 2003). One of the main effects, determining regimes of interaction and efficiency of laser energy absorption, is the formation of a critical density layer of plasma near the surface. This layer screens the penetration of the laser radiation into the target volume and limits the absorption efficiency of the laser energy. The formation of the pre-plasma layer is directly linked to the temporal contrast in the laser pulse. CPA-based high-power laser systems suffer relatively low temporal contrast of laser pulse arising from the amplified spontaneous emission (ASE) and pre-pulses generated during the amplification process (Keppler *et al* 2016). The ASE and pre-pulses are interacting with the target on a nanosecond/picosecond timescale leading to expansion (melting and ionization) of the target surface long before the arrival of the main pulse.

A typical technique to improve the temporal contrast is by frequency doubling of the laser radiation. However, the advantage of using frequency doubling for contrast cleaning is compromised by a reduction in the laser pulse energy (thus intensity) due to the low conversion efficiency of the Second Harmonic Generation (SHG) process for femtosecond pulses as well as by shortening the wavelength. The consequence of wavelength reduction is a relatively low effective temperature of hot electrons due to quadratic scaling with the laser wavelength according to $T_{hot} = [1 + I\lambda_{\mu}^2/1.4 \times 10^{18}] \times 511keV$, where I is in W/cm^2 and λ_{μ} is in microns (μm) (Wilks 1993, Rosmej *et al* 2018). Simultaneously, the normalized vector potential, which specifies the regime of interaction, $a_0 = 0.85 \times 10^{-9}\sqrt{I}\,\lambda$, with I being the laser intensity in W/cm^2 and λ the laser wavelength in microns (μm), also drops with the decrease in laser wavelength. Additionally, the reduced laser energy by frequency conversion also diminishes the laser intensity and then subsequently T_{hot} and a_0 accordingly.

In this report, we present the results of the experimental investigation of the interaction of relativistically intense, high temporal contrast ($\sim 10^{-9}$ at nanosecond-picosecond time scale) near-IR (without frequency doubling!) femtosecond laser pulses with Ti foils, employing a complex diagnostic that includes simultaneous measurements of energy spectra of electrons, protons and x-ray radiation. Furthermore, we compare the results of the measurements with our previous work which was conducted with frequency-doubled output of the same laser system, resulting in contrast improvement by several orders of magnitude (Rosmej *et al* 2018). Our results provide a reference for experiments on ultra-intense laser-solid interaction of ultrashort (femtosecond) laser pulses, generated by modern high energy laser systems with high temporal contrast. These results are especially interesting for experiments aiming at relativistic interaction with nanostructured solid targets, where issues related to the temporal contrast have critical importance. The paper is organized as follows: section 2 describes the employed experimental setup and conditions; section 3 presents experimental results on the measured electron energy and angular distribution, proton energy distribution and x-ray spectra from Ti plasma together with evaluation of plasma parameters using the generalized population kinetics and the spectral modeling code FLYCHK; section 4 presents the results of hydrodynamic simulation (HD) of the pre-plasma formation under conditions of the experimentally measured temporal laser pulse contrast and also particle-in-cell simulations of relativistic laser-plasma interaction with this pre-plasma. Finally, section 5 summarizes and concludes the obtained results.

2. Experimental setup

The experiment was carried out using the multi-terawatt Ti:Sapphire laser facility JETI-40 at the Institute of Optics and Quantum Electronics (IOQ) in Jena, Germany (FSU, IOQ Jen). The system delivers p-polarized laser pulses with an energy of ~1.2 J (before the compressor) and ~30 fs pulse duration at the central wavelength of ~800 nm. We compare experimental results for near normal incidence (15°) and for 45° focusing geometries and the corresponding experimental layouts are shown in figures 1(a), (b). The temporal contrast of pre-pulses at nanosecond-picosecond timescale was measured with a third-order cross-correlator Sequoia (Amplitude Technologies) and is shown in figure 1(c) (Almassarani *et al* 2021). The femtosecond pre-pulse at around 0.3 ns has too low intensity and does not affect the final parameters of the pre-plasma. The laser beam was focused onto the target surface for two different focusing conditions: nearly normal to the target (15°) and under oblique (45°) incidence angles using 90° and 45° Al off-axis parabolic mirrors (both having f/2.3), respectively. The laser energy on the target was measured to be around 520 mJ. The focal spot size was maintained at 3.5 μm (FWHM) and the corresponding spatial profile was optimized through an adaptive mirror in the beamline. The beam profile in the focus was measured at low energy by an imaging system including a 20x microscope objective and a CCD camera (figure 1(d)). The output energy was reduced by changing the timing in the amplification chain but keeping pump power the same as for the full energy shots. The acquired images of the intensity distribution in the focal spot were spatially integrated subsequently for accurate estimation of the peak intensity in the laser

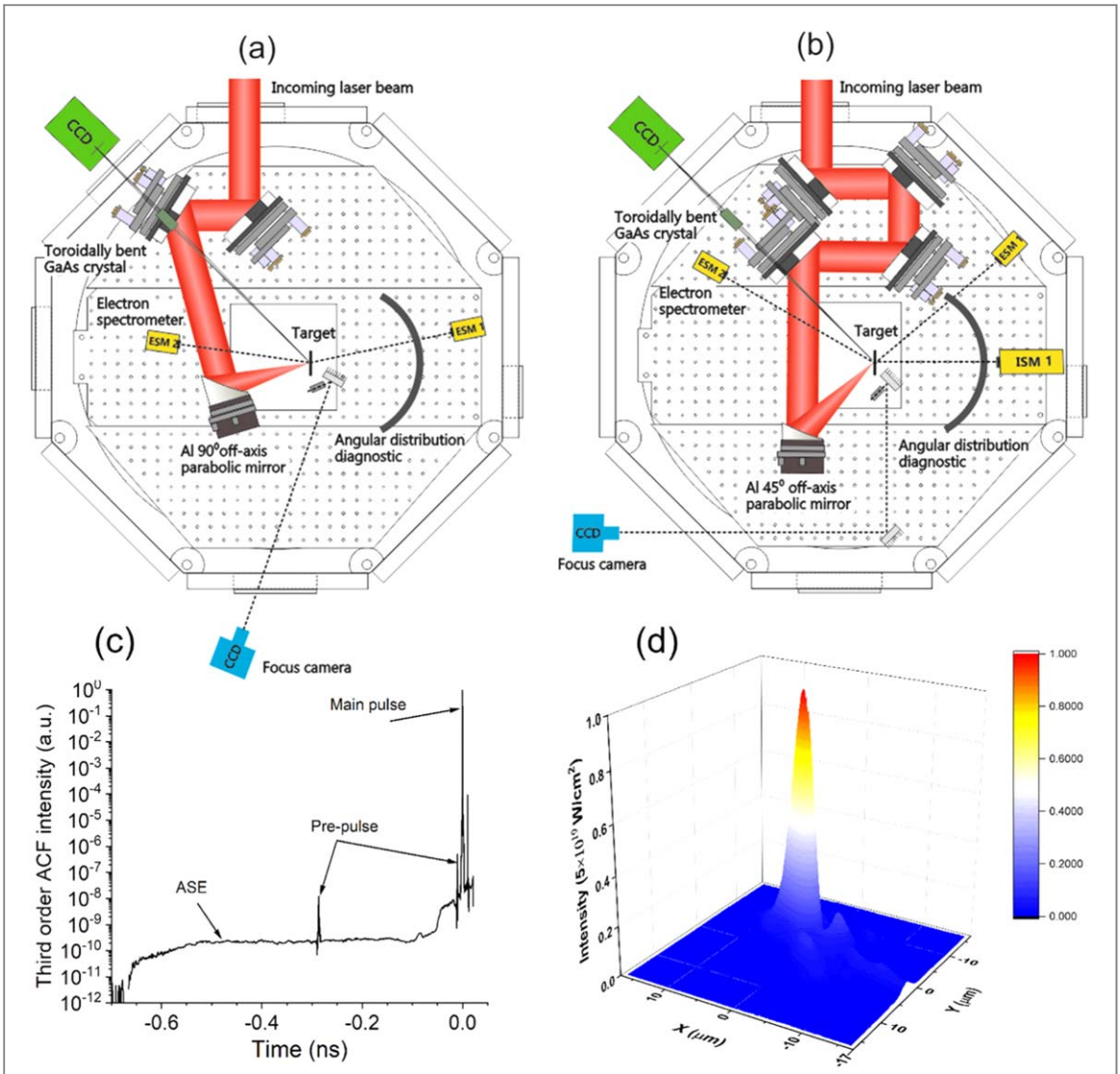

Figure 1. Schematic top view of the experimental layouts for (a) near normal and (b) 45° focusing geometries illustrating the laser beam path, focusing by the off-axis parabolic mirror onto the target and the arrangement the particle and x-ray emission diagnostics. GaAs crystal together with a CCD camera, served as an x-ray detector, were employed to measure x-ray spectra; (c) temporal contrast in the laser pulse measured by the third-order autocorrelation technique; (d) the spatial distribution of the intensity in the focal spot.

pulse. The estimated peak intensity on the target reached $\sim 5 \times 10^{19}$ W cm^{-2}, resulting in the normalized vector potential value of $a_0 \approx 5$, indicating relativistic regime of interaction, and $I\lambda^2 \approx 3.2 \times 10^{19}$ W·μm^2. The targets were 50 μm thick Ti-foils placed in a vacuum chamber.

Targets were also mounted on an XYZ-translation stage in order to ensure a fresh spot on the targets for each laser pulse as well as to align the laser focus. Moreover, it should be noted that the measurements of particle and x-ray energy spectra were accumulated over multiple shots.

In this experiment several diagnostic tools were employed in order to simultaneously detect x-rays, electrons and protons. The energy distribution of run-away electrons from the front and rear side of the targets with energies from 100 keV up to 10 MeV was measured by electron magnetic spectrometers (ESM) with magnetic field of 250 mT. Electron spectra were registered using BASF MS image plates (IP), which were absolutely calibrated in the mentioned range (Bonnet *et al* 2013, Boutoux *et al* 2015), and their measured signal was accumulated over 10 laser shots. For the near normal focusing geometry, with an angle of incidence of 15°, ESM 1 was located 27 cm behind the target in laser direction under an angle of 12° from the target normal and ESM 2 was located 33 cm from the frontside of the target in laser specular direction under an angle of 8°. For 45° focusing geometry, ESM 1 was located 30 cm behind the target again along laser propagation direction in an angle of 43°, ESM 2 was located 32 cm in front of the target again along the laser specular reflection in an angle of 30°.

An ion magnetic spectrometer (ISM) with magnetic field of 990 mT charged with BASF RS image plates (IP) was used to measure the distribution of proton energies under 45° focusing geometry behind the target. A

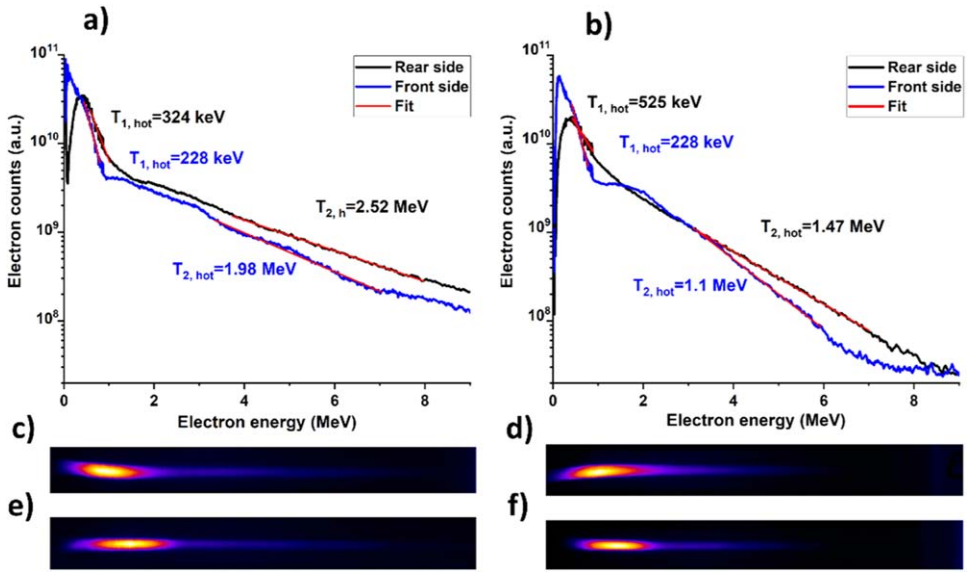

Figure 2. Energy spectra of electrons measured at the front side (blue line) and the rear side (black line) of the Ti-foil (a) near normal incidence and (b) 45° incidence geometry. At the rear side the spectra were measured in the direction of the laser beam propagation, whereas at the front side the spectra were measured under 10° for (a) and 30° for (b). The red lines correspond to the exponential fits (Maxwellian distribution) providing an estimation of the hot (T_{hot}) electron temperatures. Raw IP images obtained by the spectrometer in rear (c) and front (e) sides of target under near normal incidence geometry as well as rear (d) and front (f) sides of the target under 45° incidence geometry.

detailed description of the magnetic spectrometer was reported in (Rosmej *et al* 2019). The spectrometer was set 22 cm away from the rear side of the target in the normal direction.

For measurements of the angular distribution of accelerated electrons, a cylindrically bent BASF RS image plate with a cylinder axis on the target position and radius of curvature of 200 mm (Rusby *et al* 2015, Rosmej *et al* 2020) was used and enabled electron flux detection within a cone $\pm$ 40° in the horizontal plane relative to the laser beam direction. IPs were shielded against protons and ions by a 0.5 mm thick Copper foil. In the laser incidence plane, a central vertical 3 mm slit allowed for electron and ion energy spectra measurements behind the cylinder. The direction of laser propagation was also marked by a needle that was attached to the upper IP, as will be pointed out in the experimental results. Measurements of the angular distribution in electron flux provide insight into the dominant mechanism of laser energy absorption. Resonance (Forslund *et al* 1975) and Brunel absorption (vacuum heating) (Brunel 1987) mechanisms would result in electron acceleration predominantly along the target normal direction, whereas the $\vec{J} \times \vec{B}$ absorption mechanism (Kruer, Estabrook 1985) would generate electrons accelerated in the laser propagation direction.

The K-shell x-ray emission spectra were measured using an imaging crystal spectrometer with a charged-coupled device (CCD) as a detector. The x-ray crystal spectrometer comprised the 111 reflections of a toroidally bent GaAs crystal, with a horizontal bending radius of 1600 mm and vertical of 101 mm. Dimensions are 32 mm horizontally and 12 mm vertically and the Bragg angle for He-like titanium is 23.6°. The CCD camera was located outside the vacuum chamber, separated by a 50 μm thick Kapton window. This imaging spectrometer provides x-ray spectra with $\approx$ 2 eV spectral resolution and $\approx$ 10 μm spatial resolution.

3. Experimental results

3.1. Particle spectra and angular distribution

The measured electron spectra from both the front side and rear side (ESM 2 and ESM 1 in figure 1, respectively) of the 50 μm thick Ti-foil target for different focusing conditions are displayed in figure 2. A Maxwellian distribution function ($d^2N/(dE.d\Omega) \propto \exp(E/(k_B.T_e))$ was fitted on the spectra to estimate the temperatures of the accelerated electrons. As can be seen in the electron spectra, the first part of the hot electron temperature ($T_{1,hot}$) at the front side of the target is almost similar for both focusing conditions and estimated about 0.3 MeV, whereas it is two times higher at the rear side of the target under 45° incidence angle (~0.6 MeV).

At the same time, the second part of hot electron fraction ($T_{2,hot}$) shows two times higher temperature under the near normal focusing condition for the front (~2 MeV) and rear (<3 MeV) sides of the target in comparison to the front (~1 MeV) and rear (~1.5 MeV) sides under 45° incidence angle. Additionally, the total number of electrons generated under a near normal incidence angle is also two times higher than for the 45° incident for

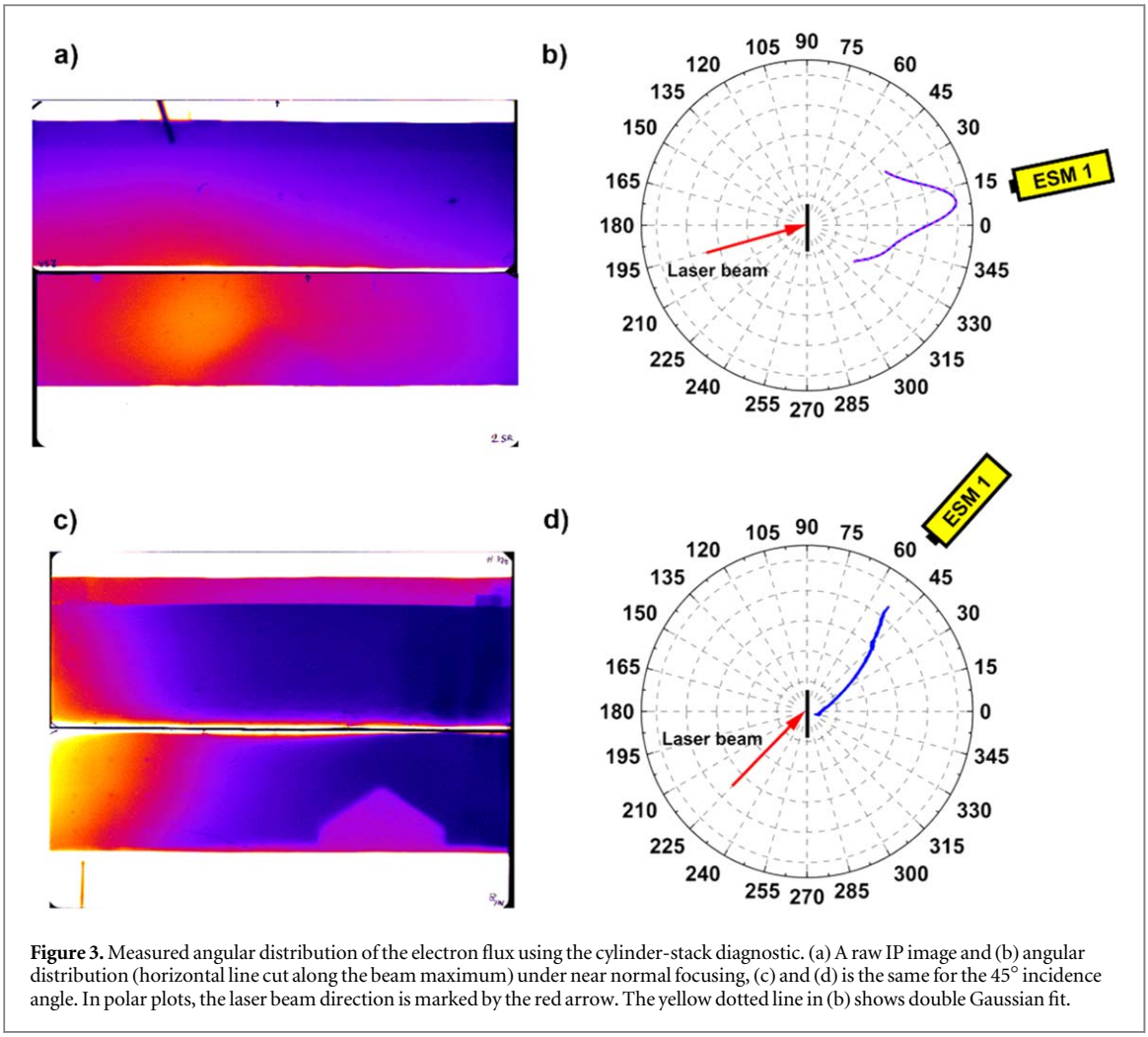

Figure 3. Measured angular distribution of the electron flux using the cylinder-stack diagnostic. (a) A raw IP image and (b) angular distribution (horizontal line cut along the beam maximum) under near normal focusing, (c) and (d) is the same for the 45° incidence angle. In polar plots, the laser beam direction is marked by the red arrow. The yellow dotted line in (b) shows double Gaussian fit.

both the front and rear sides of the target. Measured electron spectra imply that the conversion efficiency of the laser energy into the hot electrons under a near normal incidence angle is larger than for the 45° incident under our experimental conditions. The temperatures of hot electrons, generated in the forward direction along the laser propagation for both geometries, are in a good agreement with an estimation made by the Ponderomotive hot electron temperature scaling for femtosecond laser-plasma interactions. This has resulted in ~1.98 MeV for hot electron temperature for the laser parameters used in our experiment (Wilks 1993), similar to our previous experimental results at the 400 nm wavelength (frequency doubled output of the same laser system) (Rosmej *et al* 2018). An electron temperature enhancement of up to six times was observed in this experiment using 800 nm wavelength (2.52 MeV) in comparison to the experiments with 400 nm wavelength with the same Titanium targets (~0.4 MeV), in agreement with expected λ^2 scaling and lower (1.7×10^{19} W cm^{-2}) intensity used in the former case.

The angular distributions of the electron beam fluence under the near normal as well as 45° focusing conditions are displayed in figure 3. The shadow of the needle on left-side of the upper IP in figure 3 (a) and on the left-side of the lower IP in figure 3(c) shows the direction of the laser beam propagation. The half-shape of a hexagon on the lower IPs marks the normal to the target direction, corresponding to zero angle. As can be seen in figures 3(b), (d), the peak of electron distribution behind the target is almost along the laser direction for both focusing geometries.

Unfortunately, in the case of 45° incidence angle, half of the angular distribution profile was cut due to geometrical constrains in the experimental setup (mainly arising from the third dielectric mirror in figure 1(b)), preventing from accurate analysis of the width in the angular distribution. For near normal focusing the angular distribution of the electron flux can be fitted with high precision (R-square COD 0.99972) by a bi-Gaussian distribution (figure 3(b)), suggesting two electron beams with the full-cone angle of ~12° (FWHM) and ~67°.

Finally, a spectrum of protons ejected from the rear side in the normal to the target direction under 45° focusing conditions is shown in figure 4. The spectrum features a clear cut-off energy at ~1.2 MeV, suggesting the target normal sheet acceleration mechanism (TNSA) of proton acceleration. This maximum energy is in good quantitative agreement with predictions by an empiric scaling law of proton energies in ultra-short laser

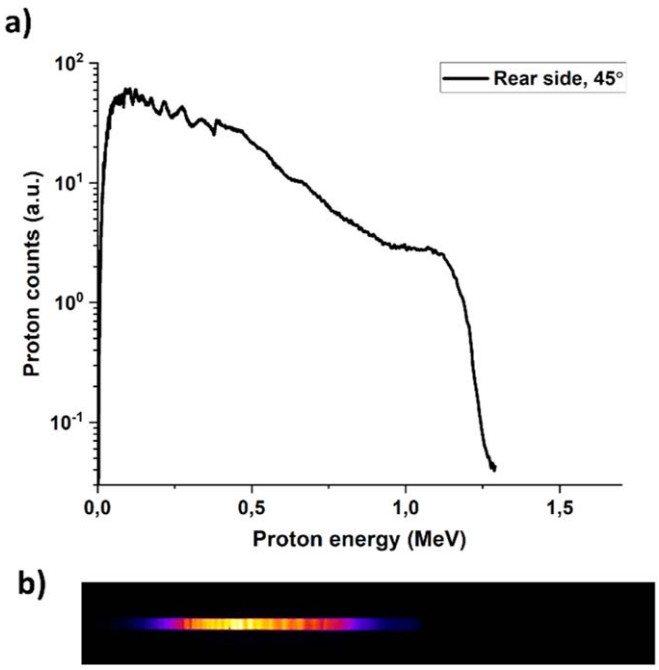

Figure 4. Energy spectra of protons, measured at the rear side of the Ti-foil in the normal to the target direction, under 45° focusing geometry (a). Raw IP images obtained by the spectrometer aligned along the laser beam direction (b).

plasma acceleration, suggested in (Zeil *et al* 2010), considering twice lower energy and three times larger foil thickness in our experiments in comparison to (Zeil *et al* 2010). Also, the maximum proton energy has been estimated using Mora's model (Mora 2003). Using the hot electron temperature 1.5 MeV, retrieved from the electron energy spectra measurements, and the laser radiation parameters, the maximum proton energy E_{max} ≈1.3 MeV is retrieved, which is in very good agreement with the measured value retrieved from the measurements.

3.2. Measured and simulated x-ray emission spectra

X-ray line emission spectra from highly charged ion states are very well suited for estimating the plasma bulk electron temperature and density (Basov 1985, Rosmej *et al* 2018, Samsonova *et al* 2019, Eftekhari-Zadeh *et al* 2022). In this experiment, the K-shell x-ray spectra of low and high charge states in the Ti plasma were used as a complementary diagnostic to the particle spectroscopy. The measured spatially resolved (in one dimension) x-ray spectra in the range of 4.5–5.0 keV, emitted from the 50 μm Ti-foil irradiated by 800 nm (1ω) laser pulses, are shown for both focusing geometries on figure 5(a) together with the spectrum, measured from a 25 μm Ti-foil, irradiated by the frequency-doubled output of the laser system (400 nm, 2ω) and $a_0 = 1.4$, (Rosmej *et al* 2018). The time and space integrated spectra are presented in figure 5(b). The spectrum in the low energy region (up to ≈ 4.55 keV, see figure 5(b)) and also above 4.9 keV consists of K-shell emission lines with satellites from Ti ions with charge states up to 12+. These emission lines, originating in overdense plasma with moderate electron temperature under influence of hot electrons, usually overlap forming a broad spectrum with a shoulder towards higher photon energies (blue shift). Analysis of this spectral region provides access to the temperature of warm dense matter (WDM)—relatively cold and low charge state plasma underneath the thin interaction layer at the surface (Stambulchik *et al* 2009, Zastrau *et al* 2010). This plasma has a much larger volume (radius and depth) than the interaction region with the laser radiation, as can be seen in figure 5(a), and is generated by fast particles, high-energy photons, and a heat wave from the interaction layer. The spatial extent of this plasma is also larger in the case of 800 nm irradiation in contrast to 400 nm irradiation (figure 5(a)). The larger size of the K-shell emission source in case of 1ω can be explained by stronger refluxing of hot electrons in Ti-foil, caused by four times higher T_{hot} than in 2ω case (Zastrau *et al* 2010, Neumayer *et al* 2010).

To estimate WDM temperature, we followed the approach developed in (Schönlein 2015). We simulated 'cold' titanium K_α doublet lines using the generalized population kinetics and the spectral modeling code FLYCHK (Chung *et al* 2005) and using the bulk plasma temperature as a fit parameter. The calculated emission lines were convoluted with the spectrometer apparatus function, described as a Voight profile with a width of 2 eV.

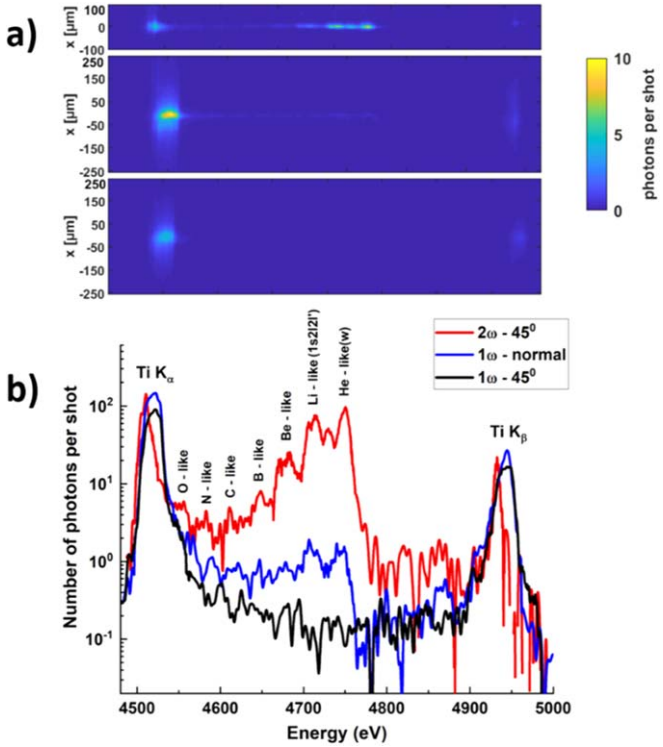

Figure 5. (a) CCD images of x-ray emission from the Ti foil, irradiated by the frequency doubled output of the laser system (400 nm, , $a_0 \approx 1.4$) (top) under 45° focusing geometry, and by the fundamental beam (800 nm, $a_0 \approx 5$) under near normal focusing (middle) and 45° focusing (bottom) geometry; (b) Corresponding calibrated single shot x-ray emission spectra.

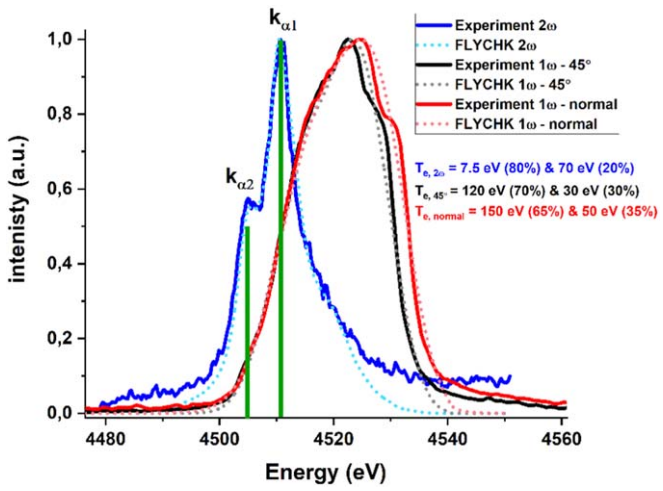

Figure 6. Comparison of measured (solid lines) and simulated (dotted) Ti Kα-line profiles for laser beams of 2ω at 1.6×10^{19} W/cm^2 laser intensity (blue line) and 1ω at 5×10^{19} W/cm^2 laser intensity under 45° (black line) and under near normal (red line) incidence angles. Positions of Kα doublet lines (Kα1 and Kα2) for a single charge Ti ion are also shown in the figure (green line). Bulk electron temperatures ($T_e^{(bulk)}$) of Ti plasmas under different experimental conditions are written in the lower box by corresponding colors as depicted in figure.

To achieve the best agreement between the measured and calculated spectra, we calculated the emission spectra for two different electronic temperatures and composed a total synthetic spectrum as a superposition of the two with different weight factors. This procedure mimics the averaging over the spatial distribution of plasma temperature that is integrated in the experimental measurements (Stambulchik *et al* 2009). Figure 6 shows a comparison of simulated line profiles and measured spectra for different experimental conditions. The simulated spectra match very well with the experimentally measured ones and result in the following values: $T_e^{(bulk)} = 120$ eV (70% fraction) + 30 eV (30% fraction) under 45° incidence angle and $T_e^{(bulk)} = 150$ eV (65% fraction) + 50 eV (35% fraction) under near normal incidence angle both with 5 eV accuracy corresponding to

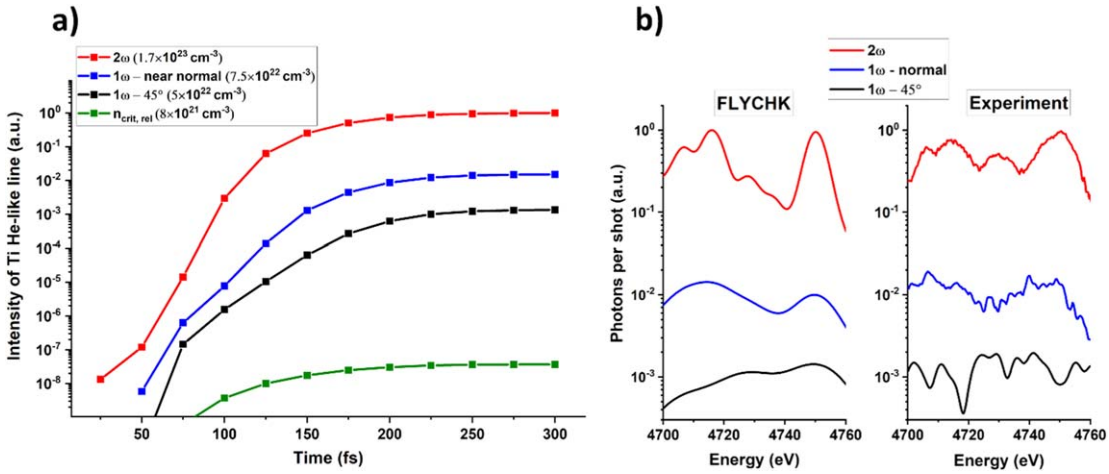

Figure 7. Time dependent evolution of the He-like line intensity in transient plasmas (a). Curves are simulated for different electron densities that were kept constant in time with a time-dependable electron temperature profile similar to 2ω case (see figure 8(a) in Rosmej *et al* (2018) see). The electron densities were chosen to obtain experimentally measured Ti He-like relative intensities 100 (2ω): 1 (1ω, 15°): < 0.1 (1ω, 45°) shown in figure 5(b); Simulated spectra of He-like(w) and Li-like Ti ions with plasma parameters, used for a) (left-hand side-FLYCHK) and also measured spectra in the same range (right-hand side-Experiment) (b).

Ti ion solid density ($n_{solid} = 5.6 \times 10^{22} cm^{-3}$) with a mean charge of $Z_i = 11$ and $Z_i = 12$, respectively. For the experiments at the second harmonic, the best agreement in simulations was achieved for the bulk electron temperature $T_e^{(bulk)} = 7.5$ eV (80% fraction) + 70 eV (20% fraction) with 2.5 eV accuracy corresponding to Ti ion solid density with a mean charge of $Z_i = 4$. Thus, we conclude that the temperature of WDM under near normal focusing conditions is about 20% higher than the temperature under 45° focusing geometry.

The spectrum between 4.55 and 4.8 keV in the high energy region is represented by resonance line emission from highly charged Ti ions of Li-like Ti^{+19}, and He-like Ti^{+20} ions (figure 5). The appearance of these high charge states in ultra-short laser-matter interaction is evidence of keV-level temperature and near-solid dense plasma, generated in the interaction layer (Rosmej *et al* 2018). As follows from figure 5, emission from He-like and Li-like Ti ions is pronounced at 1w for the case of near normal focusing (blue line in figure 5) and hardly measurable for the 45° focusing geometry. It was shown that in the 2ω case (Rosmej *et al* 2018), due to very high contrast, the relativistic laser pulse interacts with plasma of 1.7×10^{23} cm^{-3} electron density and heats it up to 1.8 keV. In the present 1ω case, due to lower temporal contrast, the pre-plasma shields the target surface, enabling penetration of the main pulse up to the relativistic critical density point. For the relativistically intense main pulse with $a_0 \approx 5$ and smooth ($L_s > \lambda$) plasma density gradient, the critical density can be estimated, according to (Weng *et al* 2012), as $n_{cr}^{rel} \approx n_{cr}\sqrt{1 + 0.79a_0^2} \approx 4.6 n_{cr}$. Detailed time-dependent analyses of the spectra evolution show nevertheless that the observed Ti^{20+}-radiation occurs in plasma with 10 × higher electron density than n_{cr}^{rel}.

Figure 7(a) shows results of time-dependent simulations of the He-like Ti-line intensity using the generalized population kinetics and the spectral modeling code FLYCHK (Chung *et al* 2005). Curves are simulated with a time-dependent electron temperature profile similar to 2ω case (see figure 8(a) in Rosmej *et al* 2018) considering in addition a small fraction of hot electrons (1% of hot electrons with the temperature 300 keV, accelerated from the plasma layer with the critical density. The temperature is taken from the experimentally measured energy distributions, see figure 2). The bulk electron density was kept constant in time and was used as a fitting parameter to match the ratios of He-like emission lines measured in the experiments with second harmonic and in the current experiment 100 : 1 for the near normal incidence and 1000 : 1 for the 45° incidence angle shown in figure 5(b). The simulations suggest densities of 1.7×10^{23} cm^{-3}, 7.5×10^{22} cm^{-3}, 5×10^{22} cm^{-3} for experiment with 2ω beam, 1ω beam with near-normal and 1ω beam with 45° incidence angles, respectively. The corresponding simulated emission spectra of He- and Li-like titanium ionic states are shown in figure 7(b) and show very good agreement with the experimentally measured spectra. Moreover, our numerical analysis suggests that the plasma density equal to the relativistic critical density $8 \times 10^{21} cm^{-3}$ is too low to produce a measurable yield at the He-like emission line as shown in figure 7(a) by green curve. Instead, order of magnitude higher density is required to reproduce the measured experimental spectra. It is noteworthy that the results of simulations are highly sensitive to the plasma density—variations on the level of several percent from the best fit values given above lead to significant disagreement between the simulated and measured spectra. In contrast, the simulation results were less sensitive to variations of temperature providing a good fit in the temperature range 1.8–3.6 keV. The reason for this is that in ultra-short laser-plasma interaction, the

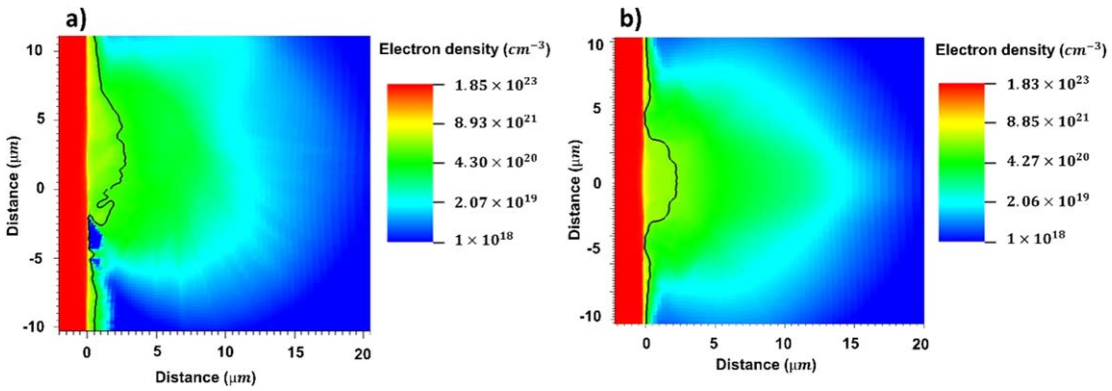

Figure 8. HD simulation of pre-plasmas generated by pre-pulses of JETI-40 laser. The laser irradiates the target from the right side. The color maps show the spatial profile of the electron density by the end of pre-pulse under 45° (a) and near normal (b) incidence angles correspondingly. Solid lines mark the non-relativistic critical density levels.

populations of ion ground states (ion charge distribution) and excited states (line radiation) grow exponentially in time with the increment defined by the electron–ion collisional rate. In addition, the line intensity is proportional to the number/density of ions with charge Z, which can be substituted by the electron density. That is why in transient plasmas the line emission intensity has very sharp dependence on the electron density. Thus, we conclude that the experimentally observed differences in the emission spectra from He-and Li-like Ti ions originate primarily from distinctly different plasma density, heated up by the laser radiation.

4. Numerical simulations

To explain the measured experimental results, complex numerical simulations of pre-plasma, generated at sub-nanosecond time scale before the peak intensity, and relativistic interaction of the main pulse with this pre-plasma and the target were carried out.

4.1. Pre-plasma simulations

To estimate parameters of the pre-plasma, generated by the laser pulses with the measured temporal contrast shown in figure (figure 1(c)), under different focusing conditions, target interaction with the laser pre-pulse was simulated using the two-dimensional (2D) radiation-hydrodynamic (HD) code RALEF2D. This code has been widely used for simulations of various experiments (Basko *et al* 2012, Tauschwitz *et al* 2013, Wagner *et al* 2014, Faik *et al* 2014, Torretti *et al* 2020, Malko *et al* 2022). RALEF-2D is a two-dimensional numerical code that solves the 2D single-fluid, one-temperature hydrodynamic equations and the spectral radiation transfer equation, using opacity tables generated with the THERMOS code (Nikiforov *et al* 2005). In our simulations, we used the equation-of-state from the equation-of-state package for high energy density matter FEOS (Faik *et al* 2018). HD simulations were performed in axial symmetry geometry using the experimental laser parameters and experimentally measured spatial laser pulse profiles. The temporal intensity in the laser radiation was scaled based on the experimentally measured temporal contrast in the laser pulse (figure 1(c)). The initial thickness of the foil was chosen at 2 μm and the foil is encased by a low-density (10^{-4} bar) gas. The equation-of-state data were constructed by using a wide-range FEOS model (Faik *et al* 2018) including the ionization degree, which is computed within the Thomas-Fermi model of the electron gas. For the near normal incidence angle, the critical density is defined as $n_{cr,0}(\lambda) = \frac{m_e \omega}{4\pi e^2} \approx 1.1 \times 10^{21} (\lambda/\mu m)^{-2}$ cm^{-3}, whereas for an incidence angle θ it becomes $n_{cr,\theta} = n_{cr,0}\ cos^2(\theta)$, where m_e is the electron mass, e is the electron charge, ω is the angular frequency. For the $\lambda = 800$ nm laser wavelength this results in critical densities of 8.5×10^{20} cm^{-3} and 1.72×10^{21} cm^{-3} for 45° and near normal incidence angles, correspondingly. As follows from figure 8, the pre-plasma generated under conditions of both focusing geometries is nearly identical. Namely, the critical density layer is in both cases located roughly 2.5 μm (3 λ) away from the target's surface.

The results of pre-plasma calculations show that it has a rather smooth gradient by the moment of the main pulse arrival. Therefore, at the value of the parameter $I\lambda^2_{\mu m} \approx 3.5 \cdot 10^{19}$ W·μm^2/cm^2 under conditions of our experiment, $\vec{J} \times \vec{B}$ is suggested as the main laser energy absorption mechanism (Wilks and Kruer 1997). This suggestion is confirmed by the simulations of relativistic main pulse interaction with the pre-plasma, presented in the following section.

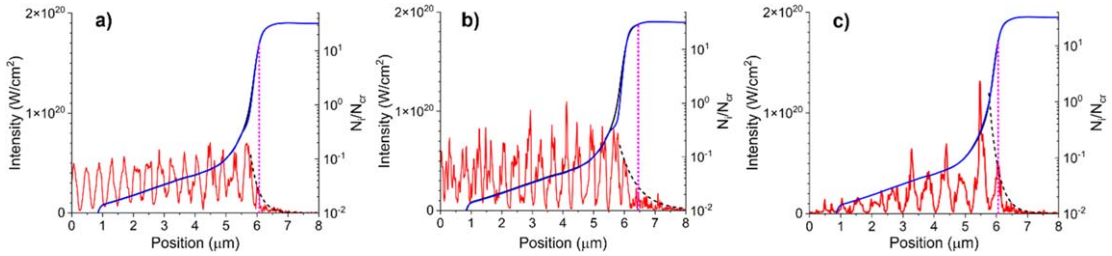

Figure 9. PIC simulations of the laser pulse intensity (red line) and the ion density (blue line) at different positions of pulse propagation. (a) Normal incidence, the peak intensity is at the target surface, (b) normal incidence, the peak intensity would be deeply inside the target, (c) 45° incidence, the peak intensity would be deeply inside the target. The black dotted line shows an exponential fit to the skinned intensity, the vertical magenta line marks the position of the e^{-1} intensity level (skin depth).

4.2. Particle-in-Cell simulations of relativistic laser-plasma interaction

To simulate the main laser pulse interaction with plasma, we used the full three-dimensional electromagnetic particle-in-cell (PIC) code VLPL (Pukhov 1999, Pukhov 2015). The simulation box size was $X \times Y \times Z = 64\ \mu\text{m} \times 40\ \mu\text{m} \times 40\ \mu\text{m}$. The grid steps were $h_x \times h_y \times h_z = 0.008\ \mu\text{m} \times 0.16\ \mu\text{m} \times 0.16\ \mu\text{m}$ and the time step $\tau = h_x/c = 26.7\text{as}$. The pre-plasma density and ionization state profile were taken from the hydrodynamic simulations of pre-plasma. The high-density part of the target has been extended over 50 μm, corresponding to the foil thickness used in the experiments, where the unperturbed titan density has been assumed with ionization state Ti^{+3}. The laser radiation is modelled as a Gaussian profile beam with the waist 3.5 μm (FWHM) and $\sin^2$ profile pulse of 30 fs duration with the peak intensity $5 \times 10^{19}\ \text{W cm}^{-2}$, thus all parameters match the experimentally measured ones. The laser pulse was propagating from along the $X-$ axis in the positive direction. The laser was $Z-$ polarized and focused on the position of the critical electron density. The PIC simulation also included the further field ionization of Titanium.

The results of simulations for evolution of the intensity in the laser pulse and the plasma density along the propagation path are shown in figure 8. Here the intensity is defined as $I(t) = c\frac{E^2+B^2}{4\pi}$ (without carrier cycle averaging) and the plasma density is the total charge density $N_i = \sum_j Z_j N_j$ where Z_j and N_j are the density and the charge number of ions with different charge states. For normal incidence, figures 9(a), (b) shows harmonic generation by the oscillating mirror mechanism (Baeva *et al* 2006) (the high frequency modulation on top of half wavelength oscillations in intensity in figure 9(b)) and steepening of the plasma density caused by the laser pulse pressure. We define the penetration point of the laser energy into the overdense plasma as the point at which the intensity starts to decay exponentially, and the corresponding decrement defines the actual skin depth. When the peak of the laser pulse arrives at the critical density position, located at $\approx$5.8 μm in figure 9(a), the skin depth is $\approx$0.277 μm and the field penetrates plasma to the point where the density reaches $\approx 10 n_{cr} \approx 2.17 n_{cr}^{rel}$. However, by the end of the laser pulse, due to the density steepening, the critical density point shifts to $\approx$5.84 μm and the skin depth increases to $\approx$0.6 μm, enabling field penetration to the point up to $\approx 30 n_{cr} \approx 6.5 n_{cr}^{rel}$ (figure 9(b)). In the case of 45° incidence focusing, no obvious steepening of the plasma density is observed, the skin depth is $\approx$0.3 μm and the field penetrates up to the point $\approx 12 n_{cr} \approx 2.6 n_{cr}^{rel}$ (figure 9(c)). Thus, we conclude that in the case of normal incidence the light pressure leads to the steepening of the plasma spatial profile and penetration of the laser energy into the region with at least twice higher plasma density than in the case of 45° incidence. The corresponding plasma density value $\approx 5.2 \cdot 10^{22}\ \text{cm}^{-3}$ is in a good agreement with the value estimated from the analysis and FLYCHK simulations of x-ray emission from He-like Ti ions. It is worth noting that the steepening is a precursor to the hole boring effect that would be expected at higher values of the $I\lambda_{\mu m}^2$ parameter ($I\lambda_{\mu m}^2 \approx 10^{20}\ \text{W}\cdot\mu\text{m}^2/\text{cm}^2$ is required for well-developed hole boring) and sharper plasma density gradients (Pukhov and Meyer-ter-Vehn 1997, Hornung *et al* 2021). Also, the difference between the plasma density profiles under normal and 45° incidence geometries can be readily explained by the twice lower normal component in the radiation pressure in the latter case.

The simulated energy spectra and the angular distribution of electron flux are shown in figure 10. For normal incidence, the calculations predict roughly equal number of electrons and electron temperature $\approx$1.5 MeV for both forward and backward directed electrons (figure 10(a)). This temperature is in a good agreement with the experimentally determined $\approx$2 MeV temperature within the same 2–9 MeV electron energy range (figure 2(a)). It is noteworthy that, as follows from our simulations, the ratio between the temperatures of forward and backward directed electrons is quite sensitive to the density gradient in the pre-plasma. For steeper gradient backward directed electrons have higher temperature than the forward directed ones, whereas the ratio reverses for smoother plasma density gradient. Thus, fairly good agreement of simulated electron energy spectra,

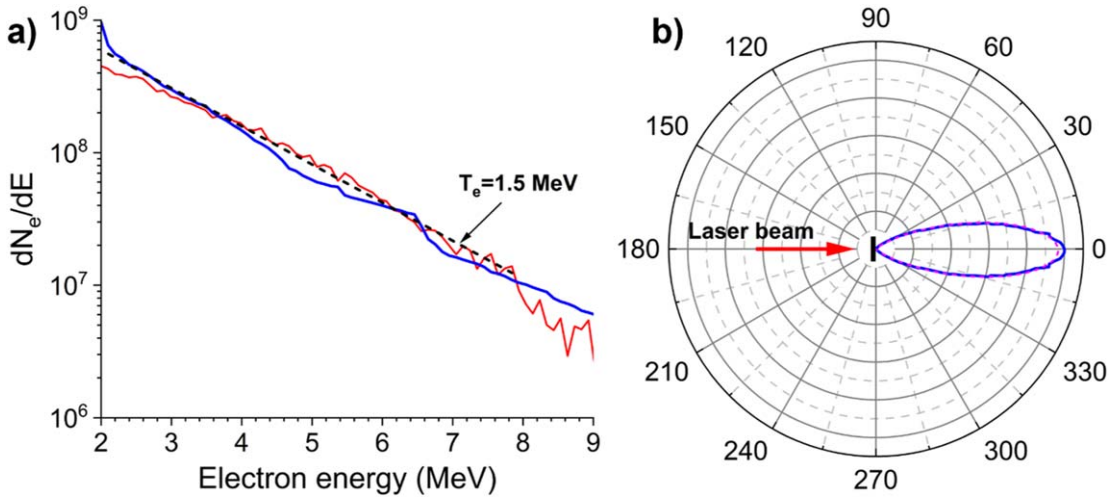

Figure 10. PIC simulations of the electron energy spectrum (a) and angular distribution of the electron flux (b) under normal focusing conditions. Red line is the energy distribution for forward directed electrons, blue line is the energy distribution for backward directed electrons. The black dashed line in (a) shows the linear fit that defines the electron temperature. The magenta dashed line in (b) shows the Gaussian fit.

suggesting roughly equal temperatures, with the measured spectra points out on good estimate of pre-plasma parameters, calculated with the 2D hydrodynamic model.

The calculated angular distribution of the electron flux suggests a well-directed along the laser beam axis, that can be fitted with high precision by a Gaussian distribution with the angular FWHM width ≈33° (figure 10(b)) . The measurements suggest bi-Gaussian distribution corresponding to a beam with ≈12° FWHM width and 67° FWHM width (see section 3.1 and figure 3). The discrepancy between the simulated and measured distributions might be explained as follows. In the experiment, the IP for electron flux measurements was covered by a 500 μm thick Cu foil. According to stopping power calculations using ESTAR database (ESTAR), only electrons with energies above 0.75 MeV would penetrate through the foil. Thus, we can expect that the low energy electrons will not contribute into the signal or will be strongly scattered within the foil, whereas high energy electrons would propagate through with minor changes in the divergence. That is why the angular distribution can be very well fitted by the two Gaussian beams. In contrast, the distribution in the numerical simulations considers all electrons emerging from the back side of the target.

5. Summary

In summary, we present the results of the experimental investigation of relativistic interaction of ultra-short laser pulses with Ti foils, employing a complex diagnostic that includes simultaneous measurements of particle and x-ray emission spectra. The interaction is investigated under two different focusing conditions: near normal to the target and under a 45° incidence angle on the target surface. We observe two times increase in hot electron temperature on both, the front and the rear, sides of the target for the near normal focusing geometry compared to 45° incidence. The spatial distribution of electrons ejected at the rear side of the target peaks in the direction of the laser beam propagation for both focusing geometries. Analysis of x-ray emission spectra suggests 1.5 times higher density of plasma generated under the near normal incidence focusing in comparison with 45° incidence angle. Detail numerical simulations of characteristic x-ray emission from Ti ions, as well as pre-plasma formation at the sub-nanosecond pre-pulse time scale and relativistic interaction of the main pulse with this pre-plasma and the target were conducted. Emission simulations, using FLYCHK population kinetic code, reproduce well the measured spectra and predict at least 1.5 times higher plasma density under near normal incidence focusing in comparison to a 45° incidence angle. Pre-plasma simulations, based on the 2D hydrodynamical model, show that insufficient temporal contrast in the laser pulse at sub-nanosecond time scale leads to pre-plasma formation with the density gradient on the scale ≈3 λ. PIC simulations of relativistic laser pulse-plasma interaction show onset of hole boring effect under normal focusing that leads to steepening of the plasma density profile and enables penetration of laser radiation deeper into the overdense plasma, where densities reach up to 30 n_{cr} (or ≈7n_{cr}^{rel}). This effect is absent for 45° incidence angle geometry and the maximum plasma density, interacting with the laser field, is about 2 times lower, what can be explained by a twice lower laser light pressure at this incidence angle. The predicted electron density, interacting with the intense laser pulse, as well as the temperature of high energy electrons, emerging in the laser propagation direction from the

rear side of the foil, and angular distribution of electron flux are in a good agreement with values, measured experimentally and estimated from spectroscopic simulations. The pre-plasma conditions and well directed along the laser beam axis spatial distribution of the electron flux, measured experimentally and reproduced in simulations, suggest that $\vec{J} \times \vec{B}$ as the major mechanism of the laser energy absorption in our experiments.

Acknowledgments

The authors acknowledge the support from the BMBF project 'BMBF-Projekt 05P21SJFA2' Verbundprojekt 05P2021 (ErUM-FSP T05). The authors also acknowledge the contributions of the JETI-40 laser team (Burgard Beleites, Falk Ronneberger, and Alexander Sävert) for running the laser system. We also acknowledge contributions supported by COST Action CA21128- PROBONO 'PROton BOron Nuclear fusion: from energy production to medical applicatiOns', supported by COST (European Cooperation in Science and Technology - www.cost.eu).

Data availability statement

All data that support the findings of this study are included within the article (and any supplementary files).

ORCID iDs

Ehsan Eftekhari-Zadeh https://orcid.org/0000-0003-1480-1450
Ingo Uschmann https://orcid.org/0000-0003-2951-4024
Alexander Pukhov https://orcid.org/0000-0001-5043-960X
Olga Rosmej https://orcid.org/0000-0003-0447-3510
Christian Spielmann https://orcid.org/0000-0002-5223-4170
Daniil Kartashov https://orcid.org/0000-0002-3227-6672

References

Almassarani M, Meng S, Beleites B, Ronneberger F, Paulus G G and Gopal A 2021 Parametric study of proton acceleration from laser-thin foil interaction *Plasma.* **4** 670–80
Baeva T, Gordienko S and Pukhov A 2006 Theory of high-order harmonic generation in relativistic laser interaction with overdense plasma *Phys. Rev. E* **74** 046404
Basko M M, Sasorov P V, Murakami M, Novikov V G and Grushin A S 2012 One-dimensional study of the radiation-dominated implosion of a cylindrical tungsten plasma column *Plasma Phys. Control. Fusion* **54** 055003
Basov N G 1985 Editor's foreword *Journal of Soviet Laser Research* **6** 81–2
Bonnet T, Comet M, Denis-Petit D, Gobet F, Hannachi F, Tarisien M, Versteegen M and Aléonard M M 2013 Response functions of imaging plates to photons, electrons and 4He particles *Rev. Sci. Instrum.* **84** 103510
Boutoux G, Rabhi N, Batani D, Binet A, Ducret J E, Jakubowska K, Nègre J P, Reverdin C and Thfoin I 2015 Study of imaging plate detector sensitivity to 5-18 MeV electrons *Rev. Sci. Instrum.* **86** 113304
Brunel F 1987 Not-so-resonant, resonant absorption *Phys. Rev. Lett.* **59** 52
Bulanov S V and Khoroshkov V S 2002 Feasibility of using laser ion accelerators in proton therapy *Plasma Phys. Rep.* **28** 453–6
Chang H X, Qiao B, Huang T W, Xu Z, Zhou C T, Gu Y Q, Yan X Q, Zepf M and He X T 2017 Brilliant petawatt gamma-ray pulse generation in quantum electrodynamic laser-plasma interaction *Sci. Rep.* **7** 1–8
Chung H K, Chen M H, Morgan W L, Ralchenko Y and Lee R W 2005 FLYCHK: Generalized population kinetics and spectral model for rapid spectroscopic analysis for all elements *High Energy Density Phys.* **1** 3–12
Eftekhari-Zadeh E, Blümcke M S, Samsonova Z, Loetzsch R, Uschmann I, Zapf M, Ronning C, Rosmej O N, Kartashov D and Spielmann C 2022 Laser energy absorption and x-ray generation in nanowire arrays irradiated by relativistically intense ultra-high contrast femtosecond laser pulses *Phys. Plasmas* **29** 013301
ESTAR (https://physics.nist.gov/PhysRefData/Star/Text/ESTAR.html)
FSU, IOQ Jena see (https://hi-jena.de/en/helmholtz_institute_jena/about-the-helmholtz-institute-jena/experimental_facilities/local/jeti40-laser/ for 'Lasersystem JETi 40')
Faik S, Tauschwitz A, Basko M M, Maruhn J A, Rosmej O, Rienecker T, Novikov V G and Grushin A S 2014 Creation of a homogeneous plasma column by means of hohlraum radiation for ion-stopping measurements *High Energy Density Phys.* **10** 47–55
Faik S, Tauschwitz A and Iosilevskiy I 2018 The equation of state package FEOS for high energy density matter *Comput. Phys. Commun.* **227** 117–25
Forslund D W, Kindel J M, Lee K, Lindman E L and Morse R L 1975 Theory and simulation of resonant absorption in a hot plasma *Phys. Rev.* A **11** 679
Higginson A *et al* 2018 Near-100 MeV protons via a laser-driven transparency-enhanced hybrid acceleration scheme *Nat. Commun.* **9** 1–9
Hornung J, Zobus Y, Roeder S, Kleinschmidt A, Bertini D, Zepf M and Bagnoud V 2021 Time-resolved study of holeboring in realistic experimental conditions *Nat. Commun.* **12** 6999
Huang M, Quevedo H J, Zhang G and Bonasera A 2019 Nuclear astrophysics with lasers *Nuclear Physics News.* **29** 9–13
Karsch L, Beyreuther E, Enghardt W, Gotz M, Masood U, Schramm U, Zeil K and Pawelke J 2017 Towards ion beam therapy based on laser plasma accelerators *Acta Oncol.* **56** 1359–66

Kemp A J, Fiuza F, Debayle A, Johzaki T, Mori W B, Patel P K, Sentoku Y and Silva L O 2014 Laser–plasma interactions for fast ignition *Nucl. Fusion* **54** 054002
Keppler S, Sävert A, Körner J, Hornung M, Liebetrau H, Hein J and Kaluza M C 2016 The generation of amplified spontaneous emission in high-power CPA laser systems *Laser Photonics Rev.* **10** 264–77
Kruer W and Estabrook K 1985 J× B heating by very intense laser light *The Physics of fluids.* **28** 430–2
Kumar G R 2010 High energy density science with tabletop terawatt lasers *In Journal of Physics: Conference Series* (San Francisco, CA, United States: IOP Publishing) 244, 012008 Bristol
Ledingham K W, Galster W and Sauerbrey R 2007 Laser-driven proton oncology—a unique new cancer therapy? *The British journal of radiology.* **80** 855–8
Ma Z, Lan H, Liu W, Wu S, Xu Y, Zhu Z and Luo W 2019 Photonuclear production of medical isotopes 62, 64Cu using intense laser-plasma electron source *Matter and Radiation at Extremes.* **4** 064401
Macchi A, Borghesi M and Passoni M 2013 Ion acceleration by superintense laser-plasma interaction *Rev. Mod. Phys.* **85** 751
Malko S *et al* 2022 Proton stopping measurements at low velocity in warm dense carbon *Nat. Commun.* **13** 1–2
Mora P 2003 Plasma expansion into a vacuum *Phys. Rev. Lett.* **90** 185002
Neumayer P *et al* 2010 The role of hot electron refluxing in laser-generated K-alpha sources *Phys. Plasmas* **17** 103103
Nikiforov A F, Novikov V G, Uvarov V B and Uvarov V B 2005 *Quantum-Statistical Models of Hot Dense Matter: Methods for Computation Opacity and equation of State* (Basel, Switzerland: Springer Science & Business Media)
Parigger C G 2020 Laser-plasma and stellar astrophysics spectroscopy *Contrib. Astron. Obs. Skalnaté Pleso.* **50** 15–31
Pukhov A 1999 Three-dimensional electromagnetic relativistic particle-in-cell code VLPL (Virtual Laser Plasma Lab) *J. Plasma Phys.* **61** 425–33
Pukhov A 2015 Particle-in-cell codes for plasma-based particle acceleration arXiv:1510.01071
Pukhov A and Meyer-ter-Vehn J 1997 Laser hole boring into overdense plasma and relativistic electron currents for fast ignition of ICF targets *Phys. Rev. Lett.* **79** 2686
Rosmej O N *et al* 2018 Generation of keV hot near-solid density plasma states at high contrast laser-matter interaction *Phys. Plasmas* **25** 083103
Rosmej O N *et al* 2019 Interaction of relativistically intense laser pulses with long-scale near critical plasmas for optimization of laser based sources of MeV electrons and gamma-rays *New J. Phys.* **21** 043044
Rosmej O N *et al* 2020 High-current laser-driven beams of relativistic electrons for high energy density research *Plasma Phys. Control. Fusion* **62** 115024
Roth M *et al* 2001 Fast ignition by intense laser-accelerated proton beams *Phys. Rev. Lett.* **86** 436
Rousse A *et al* 2004 Production of a keV x-ray beam from synchrotron radiation in relativistic laser-plasma interaction *Phys. Rev. Lett.* **93** 135005
Rusby D R *et al* 2015 Measurement of the angle, temperature and flux of fast electrons emitted from intense laser–solid interactions *J. Plasma Phys.* **81** 475810505
Samsonova Z *et al* 2019 Relativistic interaction of long-wavelength ultrashort laser pulses with nanowires *Phys. Rev.* **9** 021029
Schönlein A 2015 Erzeugung von intensiver Röntgenstrahlung und Materie hoher Energiedichte durch laserbeschleunigte Elektronen *Doctoral Thesis* Johann Wolfgang Goethe-Universität in Frankfurt am Main
Stambulchik E *et al* 2009 Progress in line-shape modeling of K-shell transitions in warm dense titanium plasmas *J. Phys. A: Math. Theor.* **42** 214056
Strickland D and Mourou G 1985 Compression of amplified chirped optical pulses *Opt. Commun.* **55** 447–9
Strobl M, Manke I, Kardjilov N, Hilger A, Dawson M and Banhart J 2009 Advances in neutron radiography and tomography *J. Phys. D: Appl. Phys.* **42** 243001
Tauschwitz A, Basko M, Frank A, Novikov V, Grushin A, Blazevic A, Roth M and Maruhn J A 2013 2D radiation-hydrodynamics modeling of laser-plasma targets for ion stopping measurements *High Energy Density Physics (N.Y.)* **9** 158–66
Torretti F *et al* 2020 Prominent radiative contributions from multiply-excited states in laser-produced tin plasma for nanolithography *Nat. Commun.* **11** 1–8
Umstadter D 2003 Relativistic laser–plasma interactions *J. Phys. D: Appl. Phys.* **36** R151
Wagner F, Bedacht S, Ortner A, Roth M, Tauschwitz A, Zielbauer B and Bagnoud V 2014 Pre-plasma formation in experiments using petawatt lasers *Opt. Express* **22** 29505–14
Weng S M, Mulser P and Sheng Z M 2012 Relativistic critical density increase and relaxation and high-power pulse propagation *Phys. Plasmas* **19** 022705
Wilks S C and Kruer W L 1997 Absorption of ultrashort, ultra-intense laser light by solids and overdense plasmas *IEEE J. Quantum Electron.* **33** 1954–68
Wilks S C 1993 Simulations of ultraintense laser–plasma interactions* *Phys. Fluids* B **5** 2603–8
Yogo A *et al* 2017 Boosting laser-ion acceleration with multi-picosecond pulses *Sci. Rep.* **7** 1–0
Zastrau U *et al* 2010 Temperature and K α-yield radial distributions in laser-produced solid-density plasmas imaged with ultrahigh-resolution x-ray spectroscopy *Phys. Rev.*E **81** 026406
Zeil K, Kraft S D, Bock S, Bussmann M, Cowan T E, Kluge T, Metzkes J, Richter T, Sauerbrey R and Schramm U 2010 The scaling of proton energies in ultrashort pulse laser plasma acceleration *New J. Phys.* **12** 045015